Quantitative total-body regional-blood flow assessed with ^{15}O-labeled water and Large Axial Field-Of-View PET: Determining optimal administration dose range and test-retest variability.

Hidehiro Iida[1,2] (https://orcid.org/0000-0002-7914-3068), Naoaki Ono[2] (https://orcid.org/0000-0002-7722-055X), Harri Merisaari[3,4](https://orcid.org/0000-0002-8515-5399), Aino E. Latva-Rasku[1](https://orcid.org/0000-0001-8786-9160), Nelli Tuomola[1] Jouni Tuisku[1](https://orcid.org/0000-0003-0965-9365), Tuula Tolvanen[1](https://orcid.org/0000-0002-3308-1260), Saunavaara Virva[1,5], Mueez U-Din[1](https://orcid.org/0000-0002-8242-3079), Nobuyuki Kudomi[6] (https://orcid.org/0000-0002-3456-8740), Hasan Sari[7,8], Shigehiko Kanaya[2] (https://orcid.org/0000-0002-2147-6900), Juhani Knuuti[1](https://orcid.org/0000-0003-3156-9593), Lauri Nummenmaa[1,9](https://orcid.org/orcid.org/0000-0002-2497-9757), Kirsi Virtanen[1](https://orcid.org/0000-0001-6183-4525), and Pirjo Nuutila[1] (https://orcid.org/0000-0001-9597-338X)

[1]Turku PET Centre, University of Turku and Turku University Hospital, FINLAND,
[2]Nara Institute of Science and Technology, Ikoma, JAPAN,
[3]Turku Brain and Mind Center, University of Turku, FINLAND
[4]Department of Radiology, Turku University and Turku University Hospital, FINLAND
[5]Department of Medical Physics, Turku University Hospital, Turku, Finland
[6]Kagawa University Faculty of Medicine, Kagawa, JAPAN,
[7]Deparment of Nuclear Medicine, Bern University Hospital, University of Bern, Bern, Switzerland
[8]Siemens Healthineers International AG, Zurich, Switzerland
[9]Department of Psychology, University of Turku, Finland

Address correspondence:
Hidehiro Iida
Turku PET Centre, Turku University Hospital, and University of Turku
Kiinamyllynkatu 4-8
20520 Turku
Finland
Tel: +35823130000
E-mail: hidehiro.iida@utu.fi

Short title: Total body regional blood flow

Graphical abstract

Quantitative total-body regional-blood flow assessed with ^{15}O-labeled water and Large Axial Field-Of-View PET: Determining optimal administration dose range and test-retest variability.

A typical parametric image example of K_1-flow at two maximum color scale values (MRD 85)

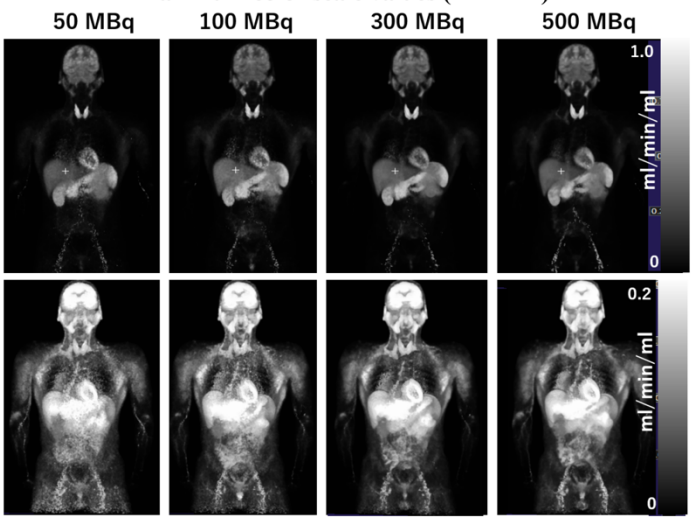

Lean: BMI 24 kg/mm2, BW 74 kg, M 48 yo

Fit procedures

- Single-tissue compartment model K_1-flow ($\alpha \cdot f$), k_2-flow (f/p), V_a), as validated in quantitative myocardial perfusion PET
- PET image-derived AIF.
- Non-linear least-square fit (increased fit convergence)
  - ➢ Parallel processing using GPU
  - ➢ Fit on the Log domain
  - ➢ Tolerance by distance ratio on the Euclidean domain

Administration dose dependence of test-retest variability (TRV)

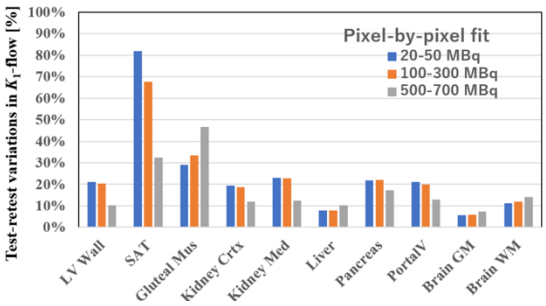

Abstract

Introduction**:** The high sensitivity of long axial field-of-view (LAFOV) PET scanners enables superior signal-to-noise ratio (SNR) and accurate quantification in low-count studies, such as ultra-low-dose or short-duration acquisitions. However, in high-count studies, their performance can be challenged by hardware limitations on total event throughput. We, therefore, investigated the acceptable dose range and test-retest variability (**TRV**) across organs when using ^{15}O-labelled water ([^{15}O]H_2O) and an LAFOV PET scanner to assess regional blood flow (***K*$_1$**-flow) in total-body organs. **Methods:** Seven volunteers (2 lean, 5 with obesity) underwent eight [^{15}O]H_2O PET scans at four different doses, from 20 to 700 MBq, totalling eight sequential PET scans at 15-minute intervals. Each dose was repeated twice for each volunteer. We examined the dose dependency across all scans and **TRV** between paired scans administered at one-hour intervals using both pixel-by-pixel and volume-of-interest (VOI)-based fitting. A single-tissue-compartment model with arterial blood volume fraction was employed without organ-specific modifications or consideration of the delay and dispersion of the arterial input function (AIF). Special attention was paid to ensure fit convergence and minimize flow-dependent bias across a wide range of ***K*$_1$**-flow values. **Results:** No evidence of critical breakdown in counting rate performance was observed even at the maximum dose of 700 MBq. **TRV** decreased with higher doses, which was consistent across pixel-by-pixel and VOI-based fitting methods. ***K*$_1$**-flow values were reliably reproduced across the dose range, with both pixel-by-pixel and VOI-based fits. **Conclusion:** The LAFOV PET scanner and [^{15}O]H_2O can generate quantitative ***K*$_1$**-flow images over a broad dose range from 20 MBq to 700 MBq, with values consistent with VOI-fit results. The best **TRV** was observed at 400-700 MBq, considerably better than previous reports.

Keywords: Large axial-field-of-PET; ^{15}O-labeled water; regional blood flow; compartment model; reproducibility; adequate administration dose range

Introduction

Large axial field-of-view (LAFOV) PET enables the simultaneous assessment of biological and physiological functions across vital organs in vivo. An increased maximum-ring distance (MRD) and fast time-of-flight markedly enhance sensitivity and improve the accuracy (*1*). The ability to directly extract the arterial input function from PET images (e.g., aorta region) is a major advantage for quantitatively assessing physiological and biological parameters without arterial blood sampling(*2*), thereby greatly simplifying logistical challenges related to correcting for delay and dispersion in arterial lines and blood sampling catheters (*3*).

^{15}O-labeled water ([^{15}O]H_2O) has been used to evaluate regional tissue flow or perfusion in various organs (*2,4-6*), based on the understanding of water molecules' diffusible nature in the interstitial space (*7-9*). A single-tissue-compartment model with arterial blood volume spill-over (***V*a**) (**STCMVa**) has been well validated for measuring myocardial blood flow (*10,11*) and has been employed for other organs (*12-15*), despite limited validation evidence.

The regional tissue time-activity curves (tTACs) for [^{15}O]H_2O vary widely in shape and absolute height across regions after intravenous (i.v.) administration, depending on tissue blood flow, ranging from 0.01 to 5.0 ml/min/ml (*2*). Due to hardware limitations, the count rate may decrease when the administered dose is too high, potentially affecting PET quantification. Conversely, the quantitative accuracy of PET images may decline if the dose is too low, due to insufficient count statistics, potentially leading to bias. PET image quality and accuracy also depend on body size, such as obesity status (*16*). Therefore, it is important to determine the lower and upper administration dose limits for [^{15}O]H_2O imaging with LAFOV PET using a reasonably well-designed program.

This study aimed to evaluate the range of administration doses that produce quantitatively acceptable $\boldsymbol{K_1}$-flow images with acceptable test-retest variability (**TRV**), suitable for clinical use. We initially evaluated the PET scanner's counting-rate performance, then examined PET image reconstruction and the software used to estimate parametric images for [^{15}O]H_2O kinetics with accelerated, accurate fit convergence.

Materials and methods

Subjects

The subjects were 7 volunteers, including 3 males and 4 females aged 21 to 60 (**Table 1**). Two subjects were of normal weight (BMI <25 kg/m²), four had class I obesity (BMI 30-34 kg/m²), and one had class III obesity (BMI=43 kg/m²). Subject details are shown in **Table 1**. The ethics committee of the Hospital District of Southwestern Finland approved the experiments and the study plan, ETMK Dnro 31/1801/2022. Written informed consent was obtained from all research subjects.

Data acquisition and processing

PET Imaging

The PET data were acquired using a Biograph Vision Quadra (Siemens Healthineers, Chicago, IL, USA) LAFOV PET/CT scanner. The administered dose ranged from 20 to 700 MBq across four levels for each subject,

from the lowest to the highest, and was repeated twice. As a result, each volunteer received eight [^{15}O]H_2O administrations: the first four (A-session) and the second four (B-session) (see **Table 1**).

Table 1. List of the subjects' backgrounds and $^{15}O[H_2O]$ administration doses.

	Sex	Age	BW	Height	BMI	Administration doses for eight scans on each subject [MBq]							
	(M/F)	(yo)	(kg)	(cm)	(kg/mm^2)	Scan 1	Scan 2	Scan 3	Scan 4	Scan 5	Scan 6	Scan 7	Scan 8
Case1	M	50	92	175	31	50	100	300	700	50	100	300	700
Case2	M	48	74	178	24	50	100	300	500	50	100	300	500
Case3	F	50	61	164	23	50	100	300	500	50	100	300	500
Case4	F	60	86	165	31	50	150	200	400	50	150	200	400
Case5*	M	21	108	186	31	20	100	300	700	20	100	300	700
Case6	F	37	124	170	43	20	200	400	700	failure	200	400	700
Case7	F	31	89	165	33	20	200	400	700	20	200	400	700
Mean ±SD	**3 M 4 F**	**42.4 ±13.4**	**90 .6 ±20.8**	**171.9 ± 8.2**	**30.9 ± 6.6**								

PET image reconstruction

The dynamic sinograms were generated from list-mode data. Time framing was 5x14s, 3x10s, 3x10s, 3x20s, 2x60s, totaling 27 frames over 420 seconds. PET images were reconstructed on the scanner console in high-sensitivity (HS) mode, using a maximum-ring distance (MRD) of 85, with ordered-subset expectation-maximization (OSEM) and PSF-TOF, with 4 iterations and 5 subsets. A 2mm Gaussian filter was applied post-reconstruction. PET data were corrected for scatter (*17,18*), CTAC attenuation, dead time, and radioactive decay. The PSF reconstruction included correction for region-specific line-spread function responses, which empirically reduces bias associated with Poisson noise (*19,20*). PET images were reconstructed using a 440×440×364 matrix, whereas CT images were reconstructed using a 512×512×364 matrix. The spatial resolution at FWHM was 3.3 mm in the radial direction, 3.4 mm in the tangential direction, and 3.8 mm in the axial direction. The TOF resolution was 228 ps at the peak noise-equivalent count rate (NECR). The sensitivity for MRD 85 was 83 cps/kBq(*1*).

Counting rate performance

Counting rate performance was evaluated using prompt, random, and net-true event rates, from which the **NECR** specific to the individual subject (*16*) was obtained for two durations: [0, 60 sec] and [60, 420 sec]. Reproducibility, obesity dependence, and the adequacy of counting rate performance were assessed.

Arterial input function

The arterial input function (AIF, $\boldsymbol{A(t)}$ [Bq/ml]) was obtained from the descending aorta region using a Carimas® v2.10 software (Turku PET Centre, Finland) and an in-house program. Approximately ten circular regions of 5 cm diameter were manually placed on transaxial planes along the descending aorta to generate a curved tube-like VOI automatically. Circular areas that show homogeneous activity distribution were identified at each slice, from which a thin tube-like VOI was defined for AIF. The VOIs were visually confirmed, and voxels were manually excluded if they were close to the border.

Computation of parametric K_1-flow

The influx flow ($\boldsymbol{K_1}$-flow [ml/min/ml]), the clearance flow ($\boldsymbol{k_2}$-flow [min^{-1}]), and arterial blood volume ($\boldsymbol{V_a}$ [ml/ml]) were estimated following the non-linear least-squares fit (NLLSF) to fit the formulation for the single-tissue compartment-model with Va (**STCMVa**), as validated for assessing regional myocardial blood flow with [^{15}O]H_2O and PET(*10,11,21,22*):

$$\boldsymbol{R}(\mathrm{t}) = \boldsymbol{K_1} \cdot \boldsymbol{A(t)} \otimes e^{-\boldsymbol{k_2} \cdot t} + \boldsymbol{V_a} \cdot \boldsymbol{A(t)} \quad \text{(eq. 1a).}$$

$\boldsymbol{K_1}$ was interpreted as(*23-25*)}:

$$\boldsymbol{K_1}\text{-flow [ml/min/ml]} = \boldsymbol{\alpha \cdot f} \quad \text{(eq. 1b),}$$

where $\boldsymbol{\alpha}$ denotes the mass of water-perfusable tissue per unit volume [g/ml], reflected by the partial volume effect (PVE), and $\boldsymbol{f}$ represents the true regional blood flow, free from PVE [ml/min per unit gram of tissue].

Programs were implemented to obtain $\boldsymbol{K_1}$-flow in 2-ways:

(a) To calculate parametric images of $\boldsymbol{K_1}$-flow, $\boldsymbol{k_2}$-flow, and $\boldsymbol{V_a}$, from which $\boldsymbol{K_1}$-flow values by averaging pixel values ('pixel-by-pixel fit'). This calculation employed parallel processing on a Graphics Processing Unit (GPU) using the gradient descent method (*26*). Parametric image calculation took 30-60 min, typically with <1000 iterations. This program was used to bootstrap and all volunteer data to assess the mean, COV, and **TRV**.

(b) To fit tTACs for VOIs to determine $\boldsymbol{K_1}$-flow, $\boldsymbol{k_2}$-flow, and $\boldsymbol{V_a}$ values ('VOI-based fit'). The fit employed the Nelder-Mead method and was applied to the volunteer images to evaluate dose dependency and **TRV** of $\boldsymbol{K_1}$-flow.

In both methods, $\boldsymbol{K_1}$-flow was obtained by ensuring that NLLSF converged across a wide range of organ-dependent flow values and tissue radioactivity concentrations. The NLLSF calculations were carried out in logarithmic space to accelerate the fit, with the tolerance (the convergence criterion) set to the relative distance in the residues to maintain consistent precision across the flow range.

Selection of volumes-of-interest (VOI)

Volumes-of-interest (VOIs) were manually outlined in Carimas® v2.10 as listed in **Table 2** on the $\boldsymbol{K_1}$-flow images obtained via pixel-by-pixel fitting. Low-dose CT images were used to verify the organ boundaries when needed. Efforts were made to adjust VOIs for apparent movement between scans (but not during scans).

Bootstrap data calculations

The bootstrap calculation was performed using a dedicated software prototype (e7-tools, Siemens Healthineers), following Dahlbom et al. (*27*), on four selected list-mode datasets at administration doses of 50, 100, 300, and 700 MBq from Case 1 in A-session. Ten replicas of the original list-mode data were generated by randomly sampling 50% of the original data for each replica. These list-mode data were histogrammed and reconstructed to

produce ten dynamic images. Ten sets of K_1-flow images were created, from which the mean and standard deviation (SD) images, and the COV, as the mean of SD divided by the mean, were calculated for each VOI.

Table 2.

List of the volumes of interest (VOIs) selected in this study. All were manually defined by two experienced clinical scientists. The table shows the order, the VOI location names, and their volumes (cm3). (**102 words**)

No	Manually-drawn ROIs	Volume (cm^3)
1	**Left ventricular (LV) wall**	14.9
2	**Subcutaneous adipose tissue (SAT)-Rt**	6.4
3	**Subcutaneous adipose tissue (SAT)-Lt**	9.1
4	**Gluteal Muscle-Rt**	25.5
5	**Gluteal Muscle-Lt**	12.5
6	**Kidney_cortex_Rt**	22.4
7	**Kidney_cortex_Lt**	24.8
8	**Kidney_medulla_Rt**	12
9	**Kidney_medulla_Lt**	19.5
10	**Liver**	88.9
11	**Pancreas**	7
12	**Poartal vein**	1.1
13	**Brain_grey-matter (GM)_Rt**	37.8
14	**Brain_grey_matter (GM)_Lt**	19.4
15	**Brain_white_matter (WM)_Rt**	1.2
16	**Brain_white_matter (WM)_Lt**	2.2

Data analysis

The administration dose and obesity-related effects on the quality of K_1-flow images were visually assessed by using a consistent maximum color scale across doses. The K_1-flow values from the pixel-by-pixel and VOI-based fits were compared across all scans and VOIs. Regression analysis was used to determine the correlation coefficients among paired K_1-flow values and to compare pixel-by-pixel and VOI-based fits across three dose ranges: 20-50, 100-300, and 400-700 MBq. A Bland-Altman analysis was used to compare the mean K_1-flow values across the grouped

dose ranges for both fit methods. Additionally, a multicomponent analysis was conducted to examine the effect of the administration dose on $\boldsymbol{K_1}$-flow values for both pixel-by-pixel and VOI-based fit methods.

The mean $\boldsymbol{K_1}$ was calculated as the average of all paired means, and the SD of all differences ($\mathbf{SD^{diff}}$) was determined, along with the COV of all the differences ($\mathbf{COV^{diff}}$) as $\mathbf{SD^{diff}}$ /Mean. The $\mathbf{COV^{diff}}$ was used as an index of **TRV** (*28*) and compared between the pixel-by-pixel and VOI-based fit methods for each VOI. The bootstrap results were used to assess whether the COV values decrease monotonically. Results are shown as Mean ± 1 SD unless noted otherwise. A paired or unpaired *t*-test was used to compare two variables, depending on the data. ANOVA was used to compare multiple groups. Pearson's correlation analysis was used to assess relationships. P-values below 0.05 were considered statistically significant.

Results

All PET scans were successfully completed except for the second manual injection of $[^{15}O]H_2O$ at 20 MBq, which failed in Case 6. The same subject exhibited the largest statistical noise. Movement was likely, but the realignment of VOI was not performed due to difficulty in the noisy environment. Considerable movement was observed in Case 5 during and between scans, along with an abnormal morphological structure in the left kidney. This subject data was used only for the count-rate analysis.

Figure 1 shows typical maximum-intensity projection (MIP) images of $\boldsymbol{K_1}$-flow with varying maximum values, demonstrating successful pixel-by-pixel calculations across a wide range of $\boldsymbol{K_1}$-flow in both a normal body-weight (**Figure 1A**) and a class III obesity (**Figure 1B**) volunteer. The arterial vessels were well removed in most areas, except the forearm and thigh.

The counting-rate performance (true, random, and NECR) showed no irregularities (**Supplementary Figure 1**) in either the normal body-weight or Class-III obesity volunteers. **Figure 3** illustrates how the patient-specific **NECR** (*16*), as an index of signal-to-noise ratio (**SNR**), varied with the administration dose for the scans: 0-60 sec and 60-420 sec, corresponding to the first (**3A and 3C)** and second (**3B and 3D**) sessions, and is reproducible for each patient. **NECR** was consistently lower in the volunteer with class III obesity (Case 6) due to reduced net true rates and larger random rates. **NECR** for 0-60 sec increased steadily to a peak. The two lean volunteers quickly reach the highest **NECR** values at 300 MBq, with only a small **NECR** increase to 500 MBq. The accumulation over the 60-420 second period increased **NECR** steadily across all data, indicating the improved **NECR** or **SNR** with a larger administration dose.

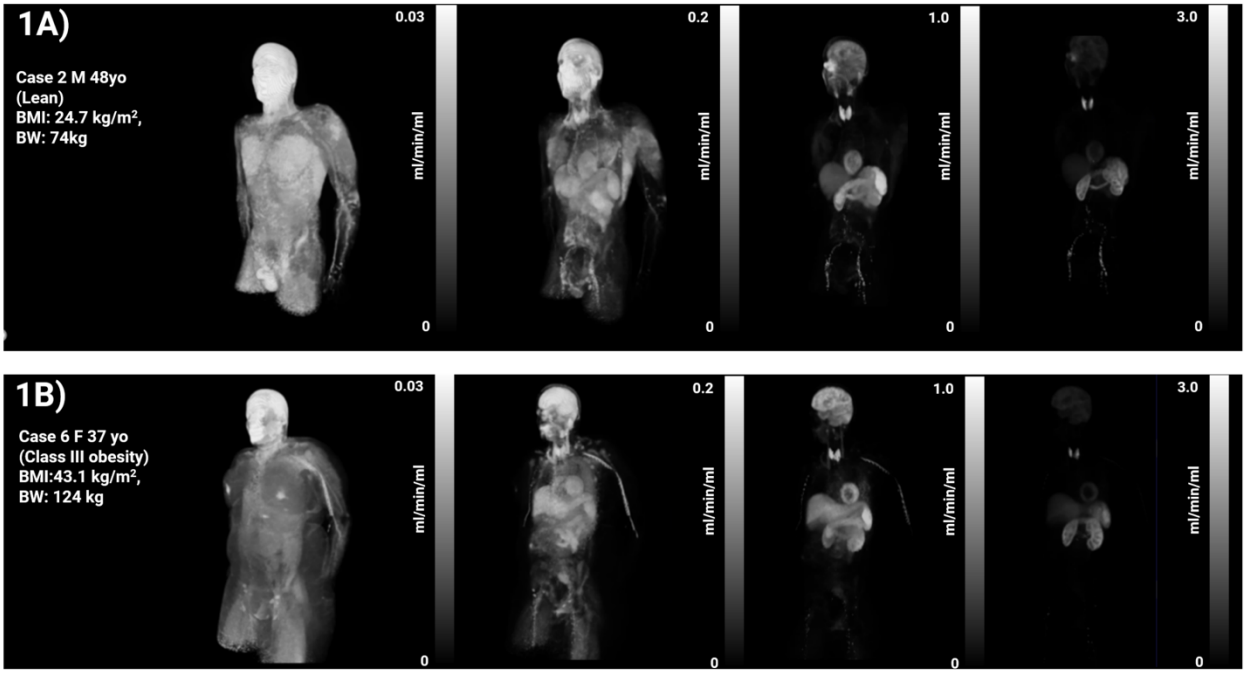

Figure 1.

Figure 1.

MIP images of K_1-flow from a normal body-weight (Case 2) (**1A**) and a class III obesity volunteer (Case 6) (**1B**), displayed with four maximum gray-scale values at 0.02, 0.2, 1.0, and 3.0 ml/min/ml for each volunteer.

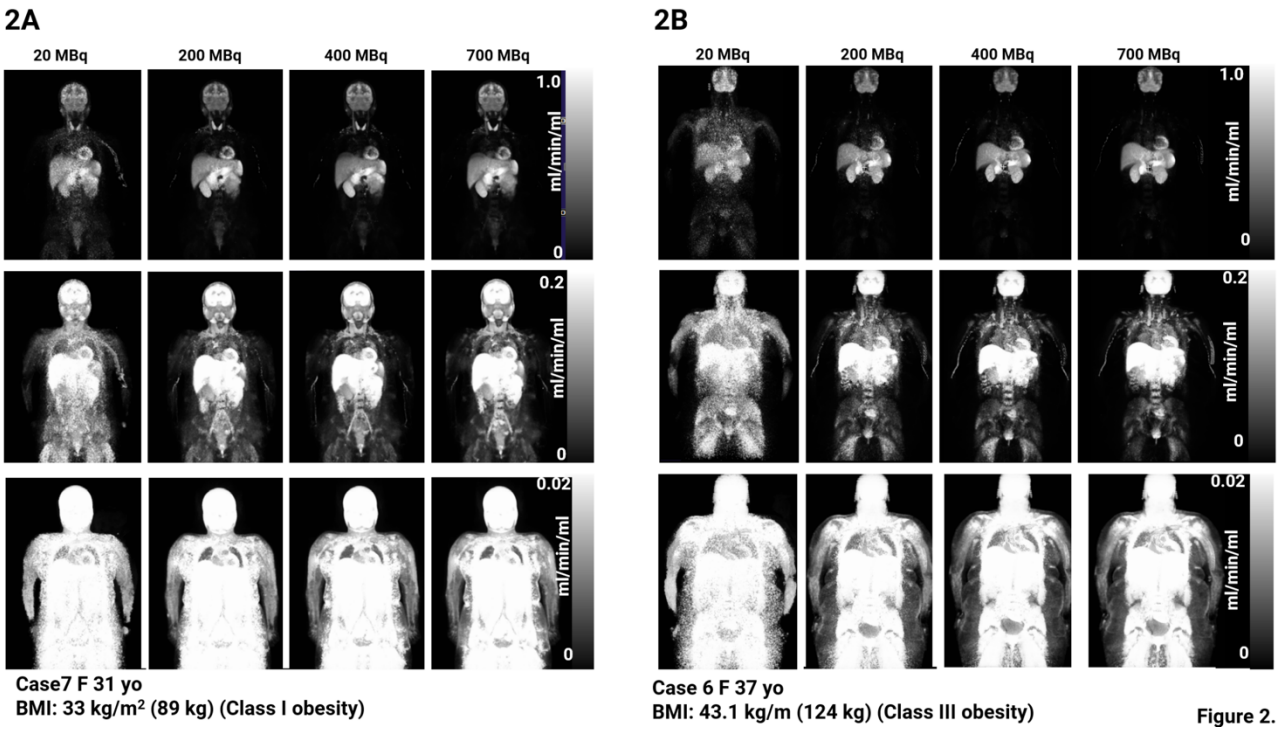

Figure 2.

Figure 2.

Coronal cross-sectional K_1-flow images from a volunteer with class I obesity (case 7) (**2A**) and a volunteer with class III obesity (Case 6) (**2B**) displayed with the maximum color scale values at 1.0, 0.2, and 0.02 ml/min/ml for varied

doses at 20, 200, 400, and 700 MBq.

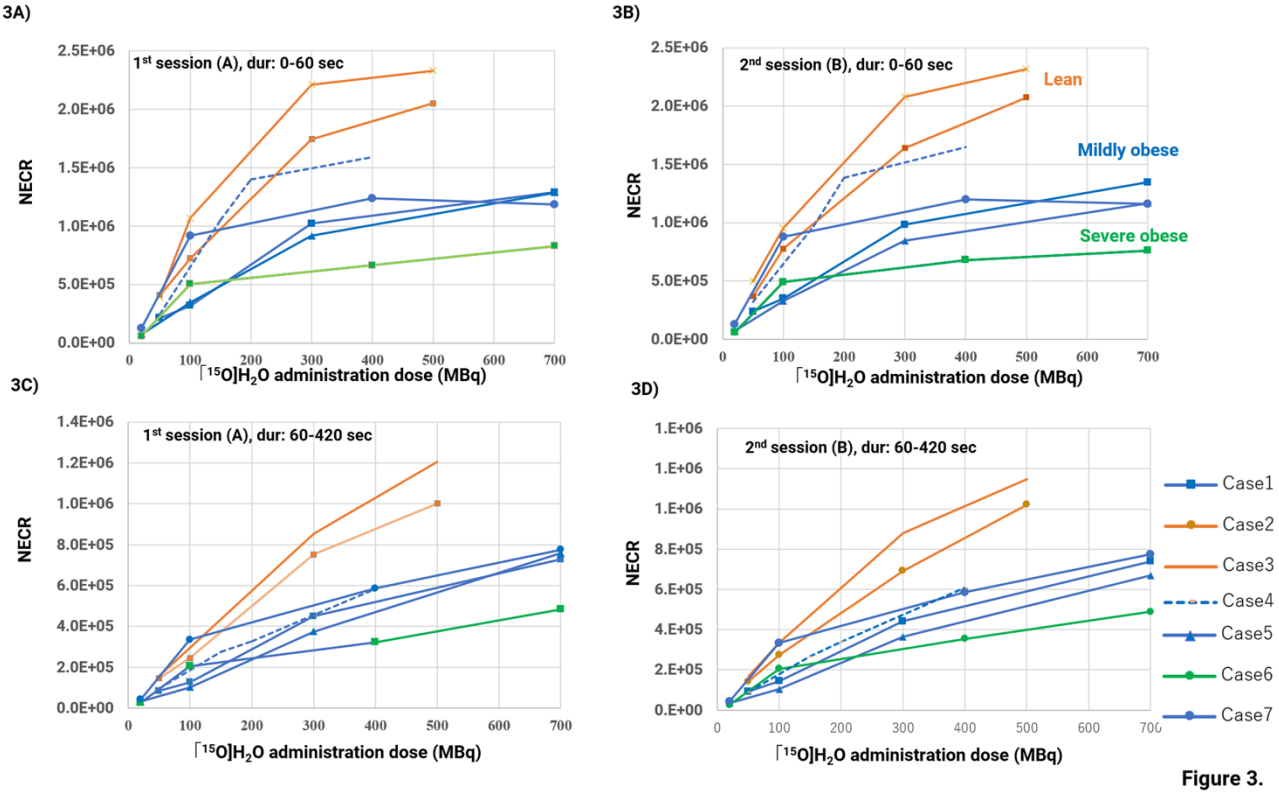

Figure 3.

Figure 3.

Comparison of **NECR** curves specific to individual patients (*16*) as a function of the administered dose, averaged over the [0-60 sec] (**3A** and **3B**) and [60-420 sec] (**3C** and **3D**) periods, obtained from all scans on all volunteers.

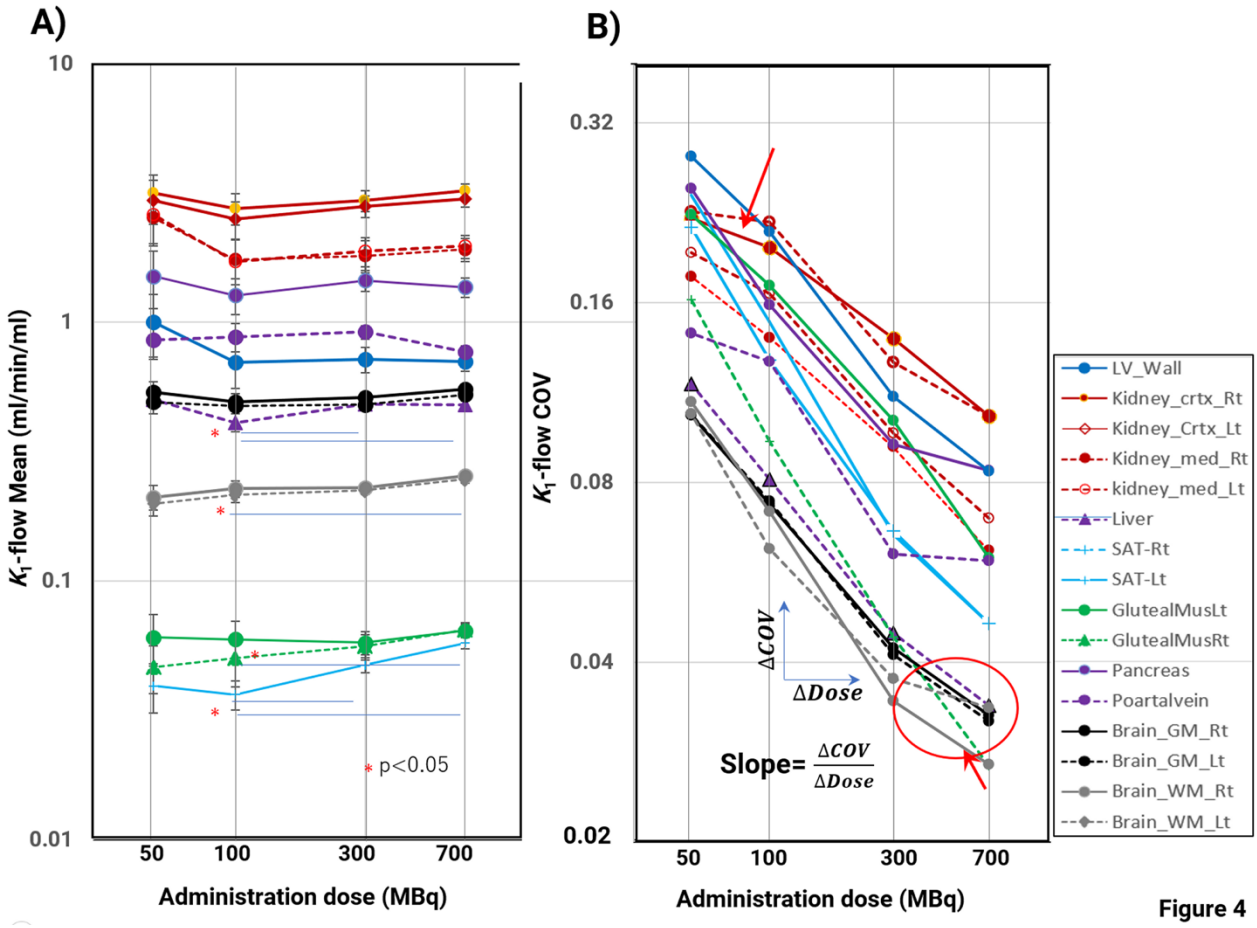

Figure 4.

Results from the Bootstrap analysis calculated using **Case 1A** data: **(4A)** Averaged K_1-flow values, and **(4B)** COV in K_1-flow, as a function of administration dose at 50, 100, 300, and 700 MBq.

Figure 5.

Comparison of K_1-flow values between the pixel-by-pixel and VOI-based fit results at a dose range of 100-300 MBq—covering all VOIs except the kidney regions (**5A**) and only the kidney cortex and medulla regions (**5B**), respectively. See also **Supplementary Table 1**.

Figure 4 shows the results of the bootstrap analysis. While the mean was unchanged, COV varied by organ, with the lowest in the brain and liver and the highest in the kidney medulla and LV wall. The COV decreased by increasing the dose, with organ-dependent slopes. The brain (gray and white matter), liver, pancreas, and LV wall showed a decline in slope from 300 to 700 MBq but remained decreased.

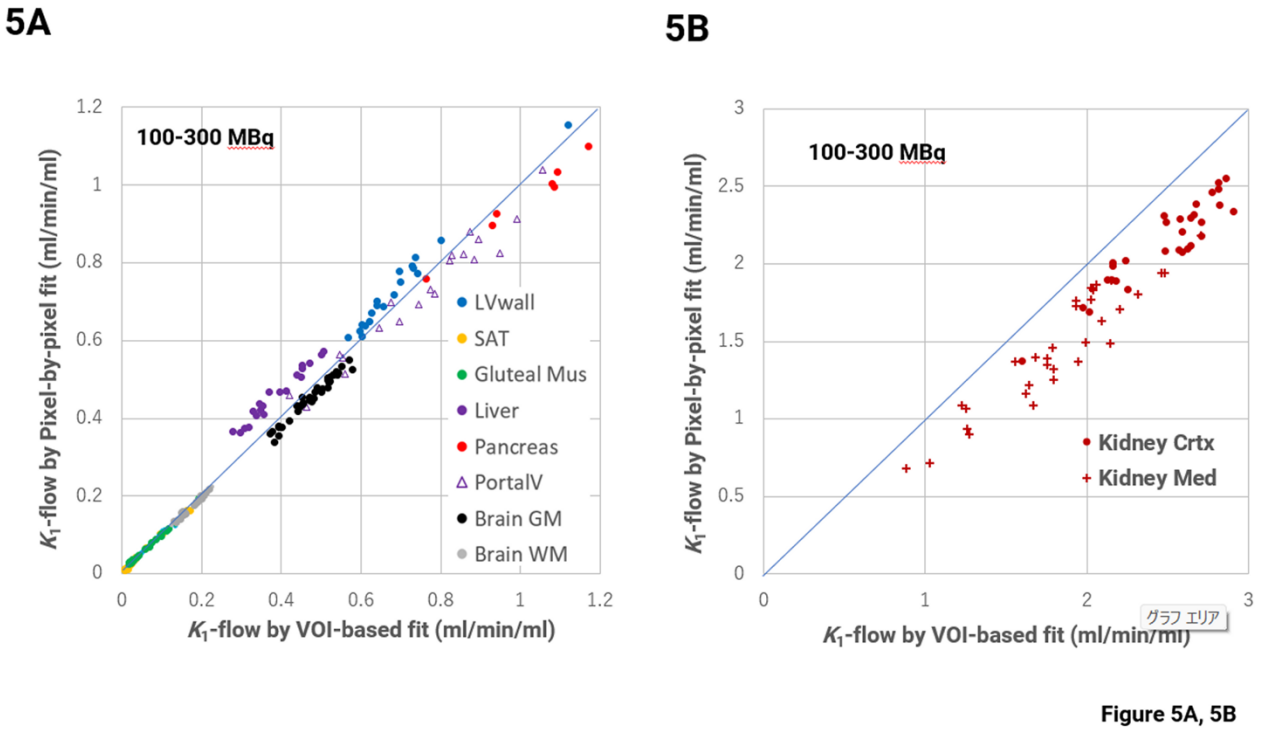

Figure 5A, 5B

Figure 5 and **Supplementary Table 1** compare K_1-flow values obtained using pixel-by-pixel with those by VOI-based fit methods at 100-300 MBq range for all organs excluding the kidney (**Figure 4A)** and specifically for kidney regions (**Figure 4B)**. Although the methods show a strong correlation, the absolute K_1-flow values differ systematically across several organs, except for the gluteal muscle region.

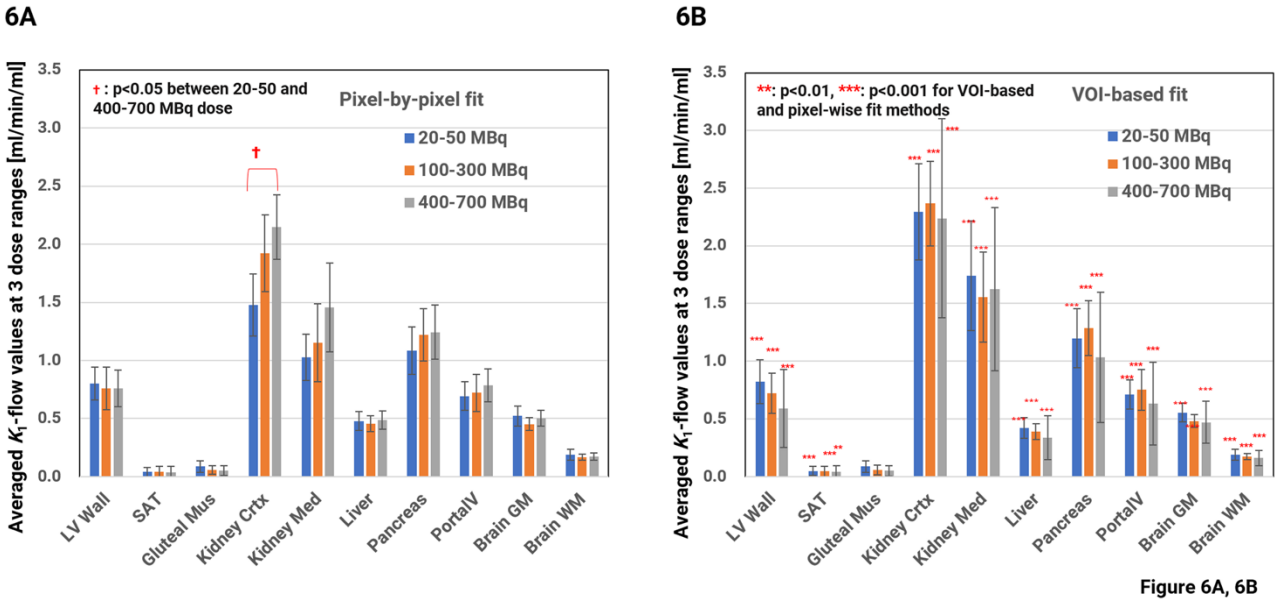

Figure 6A, 6B

Figure 6.

Summary results of the mean K_1-flow values for the three dose ranges —20-50, 100-300, and 400-700 MBq — for all VOIs, obtained with the pixel-by-pixel (**6A**) and VOI-based (**6B**) fit methods. Asterisks indicate significant differences between the two fit methods. † denotes significant difference between 20-50 and 300-700 MBq doses. See also **Supplementary Table 2**.

Figure 6 and **Supplementary Table 1** present summary results for the average K1-flow across all VOIs for the three dose ranges: 20-50, 100-300, and 400-700MBq, for both the pixel-by-pixel fit (Figure 5A) and the VOI-based fit (**Figure 5B**). No significant differences in K_1-flow values among the three dose ranges within any VOI, except for the kidney cortex. Multiple-component analysis (ANOVA) revealed no significant dose dependence in K_1-flow for either fitting approach.

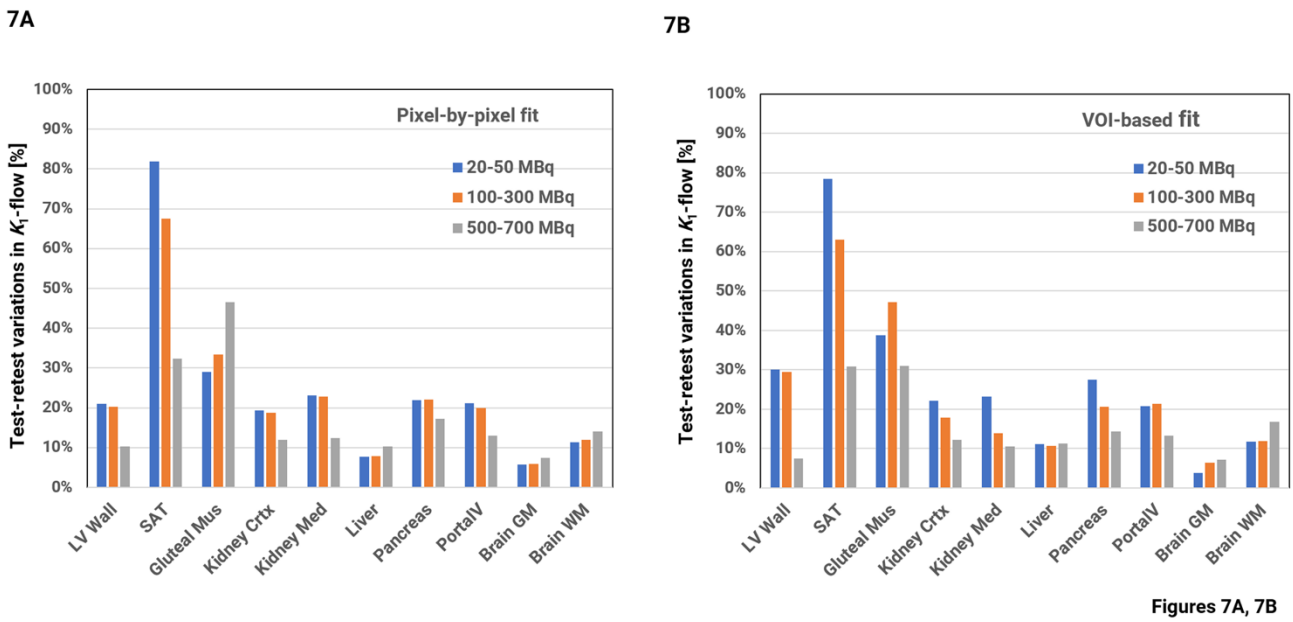

Figure 7. Summary results from the **TRV** (**COV^{diff}**) analysis using the pixel-by-pixel (**7A**) and VOI-based (**7B**) fit methods for the three dose ranges. See also **Supplementary Table 2**.

Figure 7 presents the **TRV** (**COV^{diff}**) across all VOIs observed at the three dose ranges. In the kidney cortex and medulla, pancreas, and portal vein, the **TRV** was approximately ±20% at 20-50 MBq, decreasing gradually to around 10-15% at 400-700 MBq. The brain gray matter (GM) and white matter (WM) exhibited the least variation, at 20-50 MBq, and showed a tendency to increase **TRV**, attributable to class-III obesity results.

Discussion

The goal of this study was to identify the dose range that yields unchanged quantitative K_1-flow values with minimal **TRV** across whole-body organs using [^{15}O]H_2O and LAFOV PET. The NLLSF program used in this study enabled precise fit convergence across varying doses and a wide flow range, while accelerating the fit through logarithmic-domain processing and GPU parallelization of the parametric K_1-flow image calculation. The visual assessment demonstrated superior image quality in the parametric K_1-flow images compared with images from other

recent studies obtained from the same PET scanner (*2,4-6*). Significantly increased K_1-flow in the arterial vessel regions, as shown in previous studies, diminished as seen **(Figures 1** and **2**), which was explained by the effect of improved fit convergence. Careful analysis of the count rate and **NECR** for the individual patient showed no evidence of a detector-electronics breakdown (**Figure e** and S**upplementary Figure 1**). No significant dose dependence was observed in the absolute K_1-flow values by one-way ANOVA analysis across the entire dose range in all organs, and also among the three dose ranges (20-50, 100-300, and 400-700 MBq) in all organs, with both pixel-by-pixel and VOI-based fit methods (**Figure 6**). Another important finding was that the observed **TRV** generally decreased across most organs as the dose increased, except in the brain (gray and white matter), the liver, and the gluteal muscle regions (**Figure 7**). This was consistent with the Bootstrap analysis (**Figure 4**), which showed a monotonic decrease in COV across all organs, although the slope declined from 300 to 500 MBq administration. These results also supported the adequacy of the PET image-derived AIF from the descending aorta.

There are previous studies that examined **TRV** in regional blood flow using $[^{15}O]H_2O$ and PET for the brain (*28*), myocardial wall (*29,30*), and tumors in man; however, to our knowledge, no studies examined **TRV** in other organs, nor the $[^{15}O]H_2O$ dose dependency in any organs. While **TRV** of K_1-flow was 8.9–9.1% in the middle cerebral artery (**MCA**) territory in the cerebral cortex over intervals of 3–54 days(*28*), this study demonstrated **TRV** between 3.5% and 7.5% in the same (**MCA)** region over a one-hour interval. **TRV** for myocardial blood flow (k_2-flow) (*29,30*), converted from its repeatability index, was approximately ±9.0% for the entire myocardium and ±18.5% across four segments. The k_2-flow is known to eliminate partial-volume effects, including errors due to wall motion and individual differences in myocardial wall thickness. **TRV** values for k_2-flow obtained in this study were 7.8%, 12.7%, and 5.5%, corresponding to dose ranges of 20–50, 100–300, and 400–700 MBq, respectively. The smaller **TRVs** in this study, despite a much smaller VOI size than the previous work, are reasonable given the PET scanner's higher sensitivity and count-rate performance. The myocardial wall is an exceptional organ in its uniform flow distribution, allowing selection of larger VOI sizes, which would further reduce **TRV**s. Verification is crucial if one intends to apply the k_2-flow approach to other organs.

TRVs of K_1-flow for the given **VOIs** are influenced by several factors, including statistical fluctuations in pixel values in the original dynamic PET images, errors in PET images that propagate to K_1-flow estimates, the number of pixels in the VOI, the magnitude of inhomogeneous flow distribution, the spatial resolution, and other factors. Optimal VOI sizes/shapes are practically crucial, e.g., selecting larger VOIs for better count statistics or smaller VOIs to reduce heterogeneity-associated errors.

Despite similar **TRV**, the absolute K_1-flow differed significantly across VOIs, when comparing the pixel-by-pixel and VOI-based fit results, except for the gluteal muscles (**Figure 6A vs 6B**, **Supplementary Table 1**). This could be explained, at least in part, by the heterogeneity of parametric values or the partial presence of the large V_a region within the selected VOI. Given a strong correlation in K_1-flow between the two fit methods and nearly equal **TRV** values across most organs across all dose ranges (**Figure 6** and S**upplementary Table 2**), the use of the pixel-by-pixel fit results would be reasonable for extracting quantitative K_1-flow values.

This study demonstrated the potential applicability of ultra-low-dose imaging with 20 MBq $^{15}O[H_2O]$ in

adults, except for the patient with class III obesity. Referring to a recently estimated effective dose factor for $^{15}O[H_2O]$, i.e., 0.57 μSv/MBq(*31*), a 20 MBq injection yielded 11.4 μSv effective dose. Given the reduced radiation dose, CT-based attenuation correction remains a critical limitation; thus, an alternative approach to attenuation correction is required. Of note, given the saturated **NECR** observed at 300 MBq in a normal-weight volunteer, further work is needed to determine the optimal dose for smaller-sized subjects.

There are several limitations in this study. (a) The number of subjects is limited, with only one volunteer with class III obesity participating. More data is needed. (b) Ultra-high-sensitivity (UHS) (MRD=322) data should also be evaluated, particularly for class III obesity. (c) Only the **STCMVa** kinetic model was applied across all organs, without accounting for organ-specific issues. Most likely, significant refinement is mandatory in some organs. (d) Although the effects of the AIF dispersion were known to be diminished in fitting $\boldsymbol{V_a}$ (*32*), the delay effects were only partly compensated for by the $\boldsymbol{V_a}$ fit (*33*). A preliminary simulation study demonstrated that the magnitude of delay-associated errors increases linearly with flow values, i.e., for a given delay in tTACs at 2 sec, the underestimation of $\boldsymbol{K_1}$-flow was at -0.15%, -2.0%, -4.0%, and -15% for the true $\boldsymbol{K_1}$-flow at 0.03, 0.5, and 1.0. 3.0 ml/min/ml, respectively. The delay in the arterial lines crossing in the organ is, in general, shorter than the delay of tTAC, which we consider mostly omitted by the $\boldsymbol{V_a}$ **fit.** Internal delay within the organ is significant in some organs and require further work. (f) $\boldsymbol{K_1}$-flow is a reasonable index to interpret the net influx of $^{15}O[H_2O]$ into selected VOI; its physiological significance or the adequacy for interpreting physiological function needs to be investigated in some organs.

Conclusion

The LAFOV PET with $^{15}O[H_2O]$ provided quantitative $\boldsymbol{K_1}$-flow images, from which consistent $\boldsymbol{K_1}$-flow could be obtained across whole-body organs and across a broad range of administration doses (20-700 MBq). **TRV** was improved in most organs as the dose increased, due to enhanced count statistics. The ultra-low-dose examination at 20 MBq administration is realistic.

Disclosure

The Turku University Hospital and Turku PET Centre have a research agreement with Siemens Healthineers. Juhani Knuuti received consultancy fees from GE Healthcare and Synektik and speaker fees from Siemens Healthineers, outside of the submitted work. Hasan Sari has part-time employment with Siemens Healthineers. The other authors declare that they have no competing interests.

Acknowledgments

We are grateful to the workers at the Turku PET Centre for their technical assistance. This work was supported in part by the Finnish Cultural Foundation, Instrumentarium Foundation Research Grant, the Academy of Finland, Research Council of Finland Grant, European Research Council (Advanced Grant #101141656), Jane and Aatos Erkko Foundation, Gyllenberg's Stiftelse, Japan Cardiovascular Research Foundation, and Japan Society for the Promotion of Science.

Specific contributions:

HI: Study design, parametric image calculations, data processing, and analysis. **NO**: Design and practical realization of parametric image calculation. **HM**: Bootstrap data analysis and statistical analysis. **AELR**: PET imaging and subject management. **NT**: Volume-of-interest definition, **JT:** post-processing of PET image. **TT**: Radiation-dose control, evaluation of ultra-low-dose protocol. **SV**: Quality assessment for large-dose range study. **MU**: Evaluation of parametric image quality and adequacy, **NK**: Selection of data-processing and anlysis prodecures, **HS**: PET quality assessment, **SK**: PET scanner accuracy assessment, **JK**: Study design and building the data analysis platform, LN: Assessment of study protocol, and documentation namagement, **KV**: Assessment of image quality and dose dependency, **PN**: PI, study design and ethical assessment.

Key Points:

Question: What is the acceptable administration dose range when using the short-lived ^{15}O-water with a long-axial FOV PET for quantitative assessment of total-body regional blood flow with acceptable test-retest variability?

Pertinent findings: Quantitative regional tissue flow was assessed using an image-derived input function in 7 adult volunteers with varying administered doses (20-700 MBq) at 4 levels, repeated twice. A novel software specifically designed to maximize the pixel-by-pixel fit-precision resulted in unchanged flow values with reasonable test-retest variability (8-25%) across all doses and organs with flow ranging from 0.01-3.0 mL/min/mL

Implications for patient care:

The feasibility of assessing quantitative regional blood flow as parametric images, even at administration doses of 20-50 MBq, may stimulate numerous new applications using the recent total-body PET with ^{15}O-water.

References

1. Prenosil GA, Sari H, Fürstner M, et al. Performance Characteristics of the Biograph Vision Quadra PET/CT System with a Long Axial Field of View Using the NEMA NU 2-2018 Standard. *J Nucl Med.* 2022;63:476-484.

2. Knuuti J, Tuisku J, Karpijoki H, et al. Quantitative Perfusion Imaging with Total-Body PET. *J Nucl Med.* 2023;64:11S-19S.

3. Iida H, Miura S, Shoji Y, et al. Noninvasive Quantitation of Cerebral Blood Flow Using Oxygen-15-Water and a Dual-PET System. *J Nucl Med.* 1998;39:1789-1798.

4. Ahlstrom A, Lindstrom E, Maaniitty T, et al. Automated Total-Body Perfusion Imaging with (15)O-Water PET Using Basis Functions and Organ-Specific Model Selection. *J Nucl Med.* 2025;66:1307-1313.

5. Tuisku J, Palonen S, Karpijoki H, et al. Automated long axial field of view PET image processing and kinetic modelling with the TurBO toolbox. *Eur J Nucl Med Mol Imaging.* 2026.

6. Jochumsen MR, Christensen NL, Iversen P, Gormsen LC, Sorensen J, Tolbod LP. Supplemental-Whole-body parametric mapping of tumour perfusion in metastatic prostate cancer using long axial field-of-view [(15)O]H(2)O PET. *Eur J Nucl Med Mol Imaging.* 2024;51:4134-4140.

7. Kety S, Schidt C. The nitrous oxide method for the quantitative determination of cerebral blood flow in man: theory, procedure and normal values. *J Clin Invest.* 1948;27:476-483.

8. Thews G. Implication to physiology and pathology of oxygen diffusion at the capillary level. In: Schade JP, W.H. M, eds. *Selectivity Vulnerability of the brain*. Blackwell: Oxford; 1963:pp 27-40.

9. Hazlewood UF, Rorschach HE, Lin C. Diffusion of water in tissues and MRI. *Magnetic Resonance in Medicine.* 2005;19:214-216.

10. Araujo LI, Lammertsma AA, Rhodes CG, et al. Noninvasive quantification of regional myocardial blood flow in coronary artery disease with oxygen-15-labeled carbon dioxide inhalation and positron emission tomography. *Circulation.* 1991;83:875-885.

11. Iida H, Kanno I, Takahashi A, et al. Measurement of absolute myocardial blood flow with $H_2{}^{15}O$ and dynamic positron-emission tomography. Strategy for quantification in relation to the partial-volume effect. *Circulation.* 1988;78:104-115.

12. Nuutila P, Raitakari M, Laine H, et al. Role of blood flow in regulating insulin-stimulated glucose uptake in humans. Studies using bradykinin, [^{15}O]water, and [18F]fluoro-deoxy-glucose and positron emission tomography. *J Clin Invest.* 1996;97:1741-1747.

13. Ruotsalainen U, Raitakari M, Nuutila P, et al. Quantitative blood flow measurement of skeletal muscle using oxygen-15-water and PET. *J Nucl Med.* 1997;38:314-319.

14. Honka H, Hannukainen JC, Tarkia M, et al. Pancreatic metabolism, blood flow, and beta-cell function in obese humans. *J Clin Endocrinol Metab.* 2014;99:E981-990.

15. Oguro A, Taniguchi H, Koyama H, et al. Relationship between liver function and splenic blood flow (quantitative measurement of splenic blood flow with $H_2{}^{15}O$ and a dynamic state method: 2). *Ann Nucl Med.* 1993;7:251-255.

16. Watson CC, Casey ME, Bendriem B, et al. Optimizing injected dose in clinical PET by accurately modeling the counting-rate response functions specific to individual patient scans. *Journal of Nuclear Medicine.* 2005;46:1825-1834.

17. Watson CC. New, faster, image-based scatter correction for 3D PET. *IEEE Transactions on Nuclear Science.* 2000;47:1587-1594.

18. Watson CC. Extension of Single Scatter Simulation to Scatter Correction of Time-of-Flight PET. *IEEE Trans Nucl Sci.* 2007;54:1679-1686.

19. Casey EM, Panin VY. Point spread function radial component implementation in Joseph's forward projector. United States Patent US 8,509,504 B2; 2013.

20. Panin VY, Kehren F, Michel C, Casey M. Fully 3-D PET reconstruction with system matrix derived from point source measurements. *IEEE Trans Med Imaging.* 2006;25:907-921.

21. Bergmann SR, Herrero P, Markham J, Weinheimer CJ, Walsh MN. Noninvasive quantitation of myocardial blood flow in human subjects with oxygen-15-labeled water and positron emission tomography. *J Am Coll Cardiol.* 1989;14:639-652.

22. Bremmer S, Ahlback SO, Uden R, Mellgren A. Simultaneous defecography and peritoneography in defecation disorders. *Dis Colon Rectum.* 1995;38:969-973.

23. Iida H, Rhodes CG, de Silva R, et al. Myocardial tissue fraction--correction for partial volume effects and measure of tissue viability. *J Nucl Med.* 1991;32:2169-2175.

24. Yamamoto Y, de Silva R, Rhodes CG, et al. A new strategy for the assessment of viable myocardium and regional myocardial blood flow using ^{15}O-water and dynamic positron emission tomography. *Circulation.* 1992;86:167-178.

25. de Silva R, Yamamoto Y, Rhodes CG, et al. Preoperative prediction of the outcome of coronary revascularization using positron emission tomography. *Circulation.* 1992;86:1738-1742.

26. Paszke A, Gross S, Massa F, et al. PyTorch: An Imperative Style, High-Performance Deep Learning Library. *33rd Conference on Neural Information Processing Systems (NeurIPS2019),*. Vancouver, Canada: NeurIPS; 2019:8024-8035.

27. Dahlbom M. Estimation of image noise in PET using the bootstrap method. *IEEE Transactions on Nuclear Science.* 2001;49:2062-2066.

28. Bremmer JP, van Berckel BN, Persoon S, et al. Day-to-day test-retest variability of CBF, $CMRO_2$, and OEF measurements using dynamic ^{15}O PET studies. *Mol Imaging Biol.* 2011;13:759-768.

29. Kaufmann PA, Gnecchi-Ruscone T, Yap JT, Rimoldi O, Camici PG. Assessment of the reproducibility of baseline and hyperemic myocardial blood flow measurements with ^{15}O-labeled water and PET. *J Nucl Med.* 1999;40:1848-1856.

30. Wyss CA, Koepfli P, Mikolajczyk K, Burger C, von Schulthess GK, Kaufmann PA. Bicycle exercise stress in PET for assessment of coronary flow reserve: repeatability and comparison with adenosine stress. *J Nucl Med.* 2003;44:146-154.

31. Lubberink L, Åhlström A, Maaniitty T, Tolvanen T, Sorensen J, Knuuti J. Radiation Dosimetry of ^{15}O-water Based on Dynamic Large Axial Field of View PET. *Journal of Nuclear Cardiology.* 2025;50:1071-3581.

32. Bol A, Vanmelckenbeke P, Michel C, Cogneau M, Goffinet AM. Measurement of cerebral blood flow with a bolus of oxygen-15-labelled water: comparison of dynamic and integral methods. *Eur J Nucl Med.* 1990;17:234-241.

33. Maruyama D, Iida H, Koshino K, et al. Comparative analysis of peri-nidal cerebral blood flow and metabolism using a novel quantitative (15)O-PET method in patients with arteriovenous malformations. *J Cereb Blood Flow Metab.* 2025;45:259-274.